Lateral Porous Silicon Interferometric Transducer for On-chip Flow-through Sensing Applications

Yingning He[1,2*], Douglas Silva de Vasconcellos[1*], David Bourrier[1], Kata Hajdu[1], Jean-Olivier Durand[3], Frédérique Cunin[3], Véronique Bardinal[1], and Thierry Leichlé[1,4]

[1] LAAS-CNRS, Université de Toulouse, CNRS, Toulouse, France

[2] State Key Laboratory of Molecular Engineering of Polymers, Department of Macromolecular Science, Fudan University, Shanghai, China

[3] ICGM, Univ. Montpellier, CNRS, ENSCM, Montpellier, France

[4] Georgia Tech-CNRS International Research Laboratory, School of Electrical and Computer Engineering, Atlanta, GA, USA

[*] Authors contributed equally to this work

tleichle@laas.fr , ORCID 0000-0003-3183-8976

Abstract

Most porous silicon-based interferometric sensors targeting biosensing applications consist of vertical porous silicon layers created into a silicon wafer by electrochemical anodization and operate in a flow-over configuration. In this work, we present an alternative porous silicon interferometer based on porous silicon with horizontally oriented pores. This architecture permits the integration of flow-through porous silicon membranes within planar microfluidics. Fourier-transform infrared spectroscopy was used to obtain interference spectra from fabricated lateral porous silicon membranes and red shifts were observed upon filling microfluidic chips integrating the porous membranes with solvents of higher optical indices. This work proves that lateral porous silicon membranes are typical Fabry-Pérot interferometers with a sensitivity of more than 150 nm/RIU and a limit of detection less than 10^{-3} RIU, that is comparable to vertical porous silicon layers. Moreover, we have conducted simulation studies showing that the addition of Bragg mirrors on the membranes results in spectra with narrower fringes and lateral porous silicon interferometers with improved performances. After appropriate biofunctionalization of the porous silicon surface, lateral porous silicon membrane interferometers should offer alternative solutions for the development of porous silicon flow-through biosensors monolithically integrated on-chip.

Keywords: Porous silicon; Membrane; Lab-on-a-chip; Sensor; Optical interferometer

1. Introduction

Microfluidics and the miniaturization of sensors and actuators have enabled the emergence of lab-on-a-chip (LOC) devices that integrate analytical functions on a single chip for faster/cheaper/portable analysis using smaller amounts of sample and reagents [1]. These advantages arouse great interests in developing LOC devices for point-of-care testing and medical diagnostic [2]. Sample analysis usually involves the detection of a specific biochemical compound after performing adequate sample preparation. Detection is achieved by transducing a biological recognition event into a measurable signal. The most common signal transducers include electrical, electrochemical, optical and mechanical sensors [3]. Optical sensors enable to probe surfaces and films in a nondestructive manner. The optical transduction scheme offers advantages in speed, sensitivity, and robustness, and permits in situ sensing and real-time measurements [4]. Out of the various materials available to constitute optical-based biochemical sensors, porous silicon (PSi) displays high surface area, convenient surface chemistry, biocompatibility, and has been widely studied in interferometric sensing configuration [5].

Porous silicon-based interferometric sensors consist of vertical porous silicon (VPSi) layers created into a silicon wafer, most often by silicon anodization, where the pores are oriented perpendicular to the wafer surface. Reflection of light at the top and bottom of the porous layer results in an interference pattern (Fabry-Pérot fringes) that depends on the refractive index of the porous silicon matrix, thus on the medium that fills the pores. To convert the interferometric transducer into a biosensor, the porous silicon surface is modified with probe biomolecules and recognition of molecular species by the molecular probes induces a change in the refractive index of the porous layer, giving rise to a wavelength shift in the fringe pattern.

Porous silicon biosensors have been vastly studied for sensing various elements, *e.g.* DNA, protein, enzyme activity and bacteria [6]. It is possible to carry out biosensing using porous silicon via optical measurement through a fluidic cell, as demonstrated by works where vertical porous silicon with closed-ended pores is integrated into microfluidics for real-time detection [7], [8]. However, the use of closed-ended porous silicon films results in a flow-over configuration (FO), in which the analyte solution is transported over the PSi surface, as opposed to a flow-through configuration (FT), in which the analyte solution is transported through the porous membrane. As a result, most molecules sweep past the PSi sensing region without infiltrating the porous layer, thus limiting its sensing capability. Theoretical works on nanohole array plasmonic biosensors have shown that, with similar sensor footprints, FT sensors offer around 10-fold improvement in response time for common binding kinetic analytes [9]. Besides, the experimental comparison between FO and FT sensors, later investigated

using porous silicon microcavities and free-standing membranes confirmed this significant improvement in response times, especially for large analytes due to a more efficient convective transport [10], [11]. Finally, similar studies have revealed some issues encountered with FO sensors where analytes or contaminants can be trapped within the closed-ended pores, leading to an overestimation of the sensor sensitivity [12].

Porous silicon membranes are mostly fabricated by electrochemical etching a silicon wafer, hence pores are oriented perpendicular to the wafer surface [13]. The implementation of porous silicon membranes in flow-through configurations is achieved by sandwiching free-standing membranes between two encapsulating layers with microfluidic channels, resulting in three-dimensional microfluidic systems. Such systems have several disadvantages over planar devices, among which a lack in design flexibility and simplicity when it comes to fluidic operations, the risk of fluid leaks and the difficulty to carry out direct microscope observation of the fluidic system.

To tackle these issues, we have recently developed unique processes to fabricate porous silicon membranes with open-ended lateral pores, *i.e.* with horizontal as opposed to the above described vertical pores, in order to facilitate the integration of porous membranes into planar fluidic channels. To obtain lateral porous silicon membranes (LPSi), we force the current to flow horizontally during silicon anodization. The technical implementation relies on the use of a metal electrode patterned on one sidewall of a silicon step separating two microchannels, and injecting the current to provoke electrochemical reactions on the opposite sidewall that contacts the electrolyte. Additionally, we provide electrical insulation on the top and the bottom of the step to localize pore formation within the step only. We have proposed two means for implementing the insulation of the silicon step: either by using heavily p-type doped silicon-on-insulator (SOI) wafers [14], or by sequentially implanting a thick boron and a thin phosphorus layers within lightly doped n-type bulk wafers [15]. Sealing of the microchannels separated by the silicon step with horizontal pores then resulted in the integration of a lateral porous silicon membrane into planar microfluidics. Lateral porous silicon membranes fabricated and integrated into planar fluidic chips using both processes have demonstrated filtering capability by flowing through various molecules and nanobeads using pressure-driven flow [14], [15]. The aim of the present work is to carry out interferometric measurements with lateral porous silicon membranes in order to investigate their transducing ability, as hinted in Fig. 1. Interference signals are obtained using Fourier-transform infrared spectroscopy (FTIR) on the various lateral porous silicon configurations, and despite the significant level of spectral noise due to the small footprint of the LPSi membrane, we are able to extract porosity and index of refraction values that match SEM observations. Additionally, spectral shifts are observed after filling the membrane with different solvents. Analysis of the spectra using various methods leads to the determination of the index of

refraction of the filling medium with a sensitivity of $\Delta\lambda/\Delta n_{fill} \approx 156$ nm/RIU (refractive index unit) and a limit of detection of 2 x 10^{-3} RIU, thus demonstrating the transducing ability of the LPSi membrane in a flow-through configuration, different from the flow-over configuration classically encountered with porous silicon layers with vertical pores. Finally, we conduct simulation studies showing that the addition of Bragg mirrors on the membrane leads to narrower fringes and devices with higher quality factors. After appropriate biofunctionalization of the porous silicon surface, LPSi membranes should thus offer alternative solutions for future on-chip flow-through biosensors.
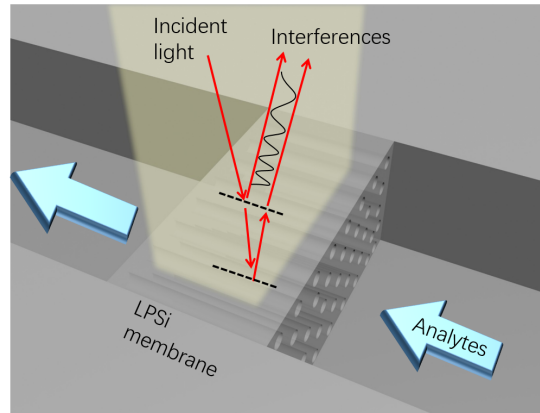

Figure 1. Schematic diagram of an on-chip lateral porous silicon (LPSi) membrane integrating an array of lateral nanopores connecting two microchannels for flow-through interferometric measurements.

2. Experimental

Local optical measurements were performed in the near infrared (NIR) range using a VERTEX 70 FTIR (Bruker Optics) equipped with a tungsten light source, a Quartz beam splitter (T502) and a Si-diode detector (SiD 510). The spectrometer was connected to a HYPERION microscope that enabled both visual observation using a 4× objective and a camera, and spectral measurements using a 36× objective (Newport corporation) with the aim to collect a maximum signal from the micron scale porous silicon membrane. The spectroscopy software OPUS was used to control the microscope and acquire data. Reflectance data acquisition was carried out with a spectral resolution of 4 cm^{-1} after taking a reference spectrum onto a gold mirror.

LPSi microfluidic chips bearing lateral porous silicon membranes were fabricated following the two processes described in [14], [15]. In the first process (SOI chips), an SOI wafer is used as the starting substrate (p type, t = 2/1/450 µm, ρ = 0.015 Ω.cm). After fabricating 2 µm deep microchannels by deep reactive ion etching (DRIE) using the buried oxide (BOX) as a stop layer, a Cr/Au metal layer (100 nm/500 nm) is sputtered onto the wafer. A thick photoresist (AZ4562 5µm thick) is patterned so as to

open a window on one of the walls of a step separating the channels. The unprotected metal is then removed by wet etching and silicon anodization is conducted in a 48% HF:1-butanol 1:1 electrolytic bath at 200 mA.cm^{-2} during 1 minute. After creating the porous silicon membrane, the metal is completely removed by wet etching and the wafer is diced into chips. The second process (implanted chips), starts by creating a $\sim$ 5 µm thick heavily doped p-layer through boron implantation (dose = 2 × 10^{15} cm^{-2}, energy = 150 KeV) in an n-type silicon wafer (ρ = 7 Ω.cm), followed by thermal annealing at 1150 °C for 8 hours. Phosphorus implantation (dose = 1 × 10^{14} cm^{-2}, energy = 50 KeV) and rapid thermal annealing (1000 °C, 5 min) are then performed to form a 150 nm thick n-type layer. The rest of the process then follows the same steps as the ones used to fabricate the SOI chips: 5 µm deep microchannels are etched by DRIE and sputtered electrodes are structured by photolithography using AZ 4562, followed by wet etching. The anodic dissolution of silicon is performed in a 3:1 mixture of HF:ethanol at 200 mA.cm^{-2} during 1 min by injecting current into the electrodes on the front of the chip. Finally, the metal is etched and the wafer is diced into chips. Each 16 mm x 16 mm fabricated chip displays either 2 or 5 µm deep microchannels (for the SOI and implanted processes, respectively), separated by a porous silicon membrane 10 µm thick (length). Additionally, VPSi chips with vertical porous silicon layers with area and thickness of 1.2 cm^2 and $\sim$ 6 µm were fabricated on a p++ silicon substrate (ρ = 0.003 Ω.cm) through silicon anodization at 160 mA.cm^{-2} during 40 s using 3:1 HF:ethanol electrolyte.

For fluidic experiments, the implanted chips are further processed: first sandblasting is used to create fluidic inlets/outlets, then the channels are encapsulated using a 500 µm thick borofloat 33 wafer (Schott) by anodic bonding. The porous silicon chips were mounted onto a sample holder which was placed on a microscope stage. The sample holder was connected to a 4-channel reservoir (FLUIWELL, Fluigent) associated with a pressure source (MFCS-8C, Fluigent) in order to easily change test solutions and to control the fluid flow inside the chip. Before injecting test solutions, the chip was exposed to oxygen plasma in order to increase the wettability of the microchannels and the nanopores.

Simulated reflectance spectra were obtained using Essential Macleod software (Thin Film Center Inc.) which is well suited for optical thin film modeling. It is based on a standard matrix formalism and takes into account the thickness and optical index (refraction and absorption) of each layer present in the vertical stack and of the silicon substrate. Index dispersion was also considered and obtained from the software database for standard materials (silicon, glass, SiO_2, Si_3N_4) or from the literature for porous silicon. The used spectral resolution was the same as the experimental one. The simulation of the optical transduction was simply done by modifying the refractive index of the lateral porous silicon layer.

3. Results and discussion

Interference spectra were first recorded with the SOI and implanted chips by focusing the microscope on the top of the LPSi membrane and downsizing the observation window to a rectangular detection area with dimensions of 10×100 μm^2 using the adjustable x- and y-apertures, where this reduced detection area is ~ 30 times smaller than the full detection area (277×277 μm^2 for the objective and detector used, according to the manufacturer), so as to only observe the LPSi membrane (see Supporting Information Fig. S1). For comparison means, reflectance spectra were also acquired with more classically used vertical porous silicon samples using the same reduced detection window for measurements. The resulting spectra are shown in Fig. 2. LPSi and VPSi samples induce interference patterns with reflectance peaks that can be adequately distinguished. As expected, LPSi membranes behave as Fabry-Pérot interferometers similarly to VPSi layers because the mean pore size, which varies between 15 ± 4 nm and 20 ± 5 nm for the implanted and the SOI chips (as estimated from the SEM images, Fig. 3), is much smaller than the imaging wavelength and thus the LPSi layer can be seen as a continuous medium.
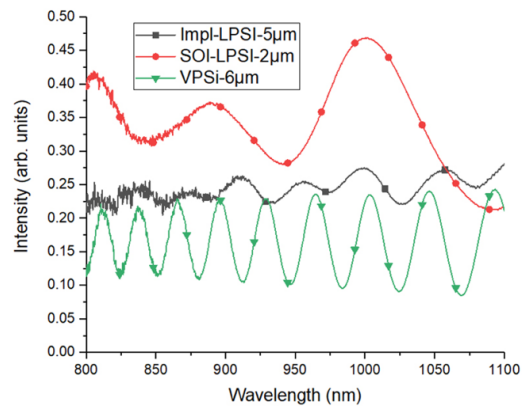

Figure 2. Reflectance spectra measured for the 2 µm SOI chip (red circles), the 5 µm implanted chip (black squares), and the 6 µm thick VPSi chip (green triangles).
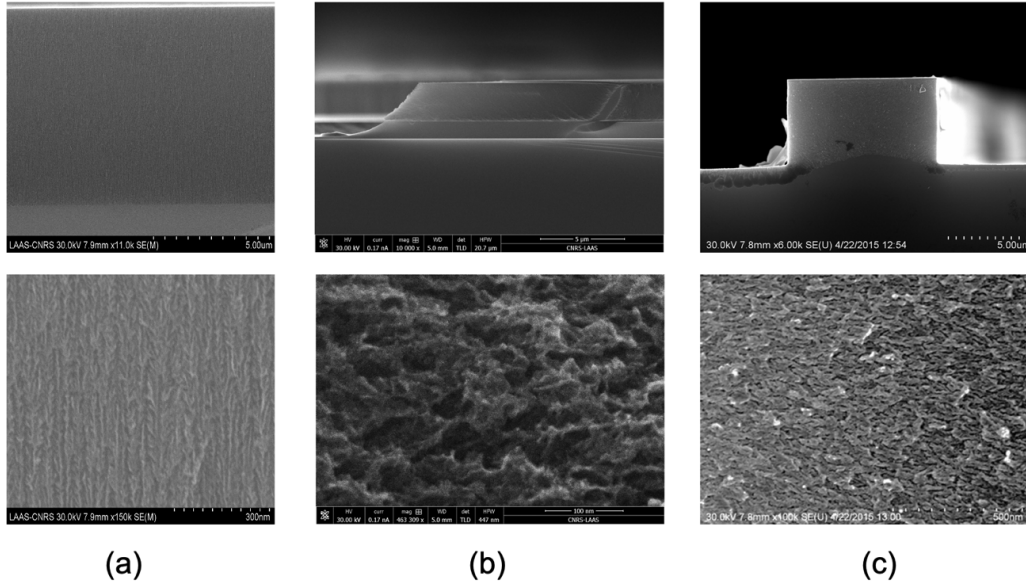
Figure 3. SEM pictures of porous silicon layers fabricated (a) on the VPSi sample, (b) the SOI chip, and (c) the implanted chip. Top: cross-section, bottom: close-up.

In the reflectance interferometric sensing configuration presented in Fig. 1, the relationship between the optical path length $2n_{layer}L\cos\theta$, also referred to as the effective optical thickness (EOT), and the Fabry-Pérot fringes is [16]:

$$2n_{layer}L\cos\theta = m\lambda_{max} \tag{1}$$

where n_{layer} and L are the refractive index and the thickness of the PSi layer, θ is the incident angle of light at the interface, m is an integer corresponding to the spectral order of the fringe and λ_{max} is the wavelength of the fringe maximum. The refractive index of the porous silicon membranes, n_{layer}, depends on the pore-filling medium as modeled by the Bruggeman effective medium theory, usually applied to porous silicon films:

$$P\frac{n_{fill}^2-n_{layer}^2}{n_{fill}^2+n_{layer}^2} + (1-P)\frac{n_{skeleton}^2-n_{layer}^2}{n_{skeleton}^2+2n_{layer}^2} = 0 \tag{2}$$

where, P is the porosity of porous silicon, and n_{fill} and $n_{skeleton}$ are the refractive indices of the medium filling the pores and of the skeleton that makes up the porous material.

We have analyzed the Fabry-Pérot fringes of Fig. 2 by Reflectometric Interference Fourier Transform Spectroscopy (RIFTS, conducted using the Fringe_24_1.pxp program available at

http://sailorgroup.ucsd.edu/software, written for the IGOR PRO software package version 8). This method computes the frequency spectrum of an input waveform by fast Fourier transform (FFT), yielding a peak whose position along the x-axis corresponds to the effective optical thickness. The FFT plots of both VPSi and implanted samples are shown in Fig. 4a (for λ > 800 nm). From the measured EOT values (respectively 25172 nm and 20255 nm), we can obtain the experimental refractive index of the porous layer using values for the membrane thickness (L) measured by SEM and $\theta = 8°$ (numerical aperture of the objective). Then, the porosity of each layer is finally calculated using equation 2, where n_{fill} and $n_{skeleton}$ are the refractive index of air and silicon. The resulting values, 54% and 41% for the VPSi and the implanted samples, respectively, are in accordance with the 55% and 40% porosities estimated from SEM images of the cross-section of the porous layers using ImageJ.
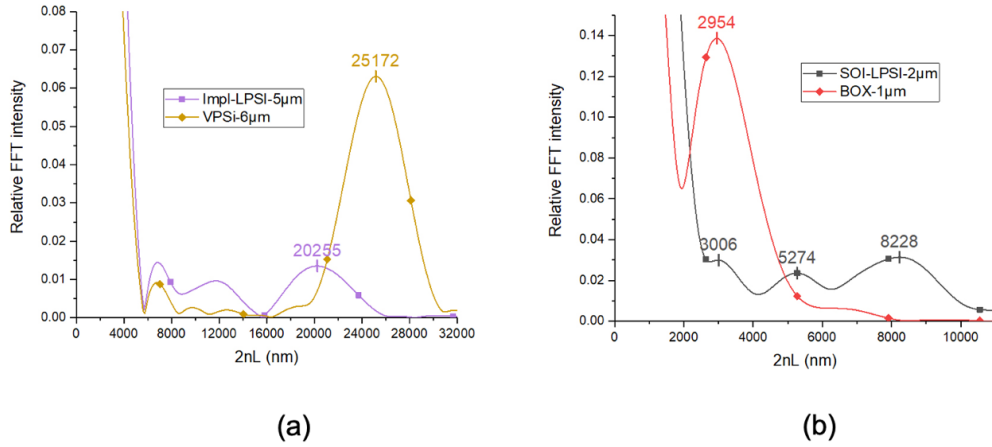

Figure 4. FFT plots of the interference spectra for (a) the VPSI and the implanted chips, and (b) for the SOI chip and the BOX layer. These plots are obtained by FFT analysis of the spectra shown in Fig. 2.

Analysis of the interference spectra for the SOI sample, which FFT plot is provided in Fig. 4b (for λ > 600 nm), is not as straightforward because this sample consists of a porous Si/SiO₂/Si multilayer: we can clearly see three distinct peaks on the FFT plot, one of which corresponds to that of the BOX layer. Another corresponds to the interferences caused by the porous layer, while the third one is due to reflections at the top of the sample and the bottom of the BOX, as predicted by theory [17]. The FFT plot of the BOX layer obtained from the reflection spectra measured on the same sample is shown in Fig. 4b and displays a 2954 nm EOT value. The peak observed at 3006 nm in the SOI FFT plot thus corresponds to the oxide layer. The second peak at 5274 nm corresponds to the 2 µm porous layer, while the third peak at 8228 nm roughly matches the added EOT values of the two other peaks and corresponds to the porous silicon/BOX double layer, which makes sense. Analysis of the second peak

gives rise of a porosity of 81% for the 2 μm porous layer that does not match the 52% estimation from the SEM image analysis: however, it should be noted that for such high porosity, we can doubt the accuracy of the image analysis method and more suitable techniques, such as gravimetry (that is however too difficult to implement on our tiny porous membrane) should be used.

Since the refractive index of the porous silicon membranes, n_{layer}, depends on the pore-filling medium as expressed by equation 2, we have tested the ability of our platform to detect a change of refractive index through reflectance interferometry by filling the bonded implanted membrane with liquids of various optical properties. The implanted LPSi device was used rather than the SOI LPSi sample because of the higher degree of confidence in the value of the porosity, as illustrated by the good fit between the observed and measured values. To this aim, evaporable solvents (water, ethanol and acetone) were sequentially injected into the LPSi membrane (see the experimental set-up in Fig. 5a). Then, following data acquisition with various solvents, the final analyte was flushed away by a continuous flow of air. To ensure the complete removal of the analyte, spectral measurements were taken during the flushing process that was carried out until the recorded spectrum corresponded to that of the empty porous silicon membrane. Fig. 5b presents the resulting reflectance spectra recorded from 800 nm to 1111 nm. Compared to empty and dried porous silicon, the presence of all three liquids clearly leads to an expected red shift of the spectrum that corresponds to an increase in refractive index of the porous layer in the following order: air (n ≈ 1) < water (n ≈ 1.33) < acetone ≈ ethanol (n ≈ 1.35).
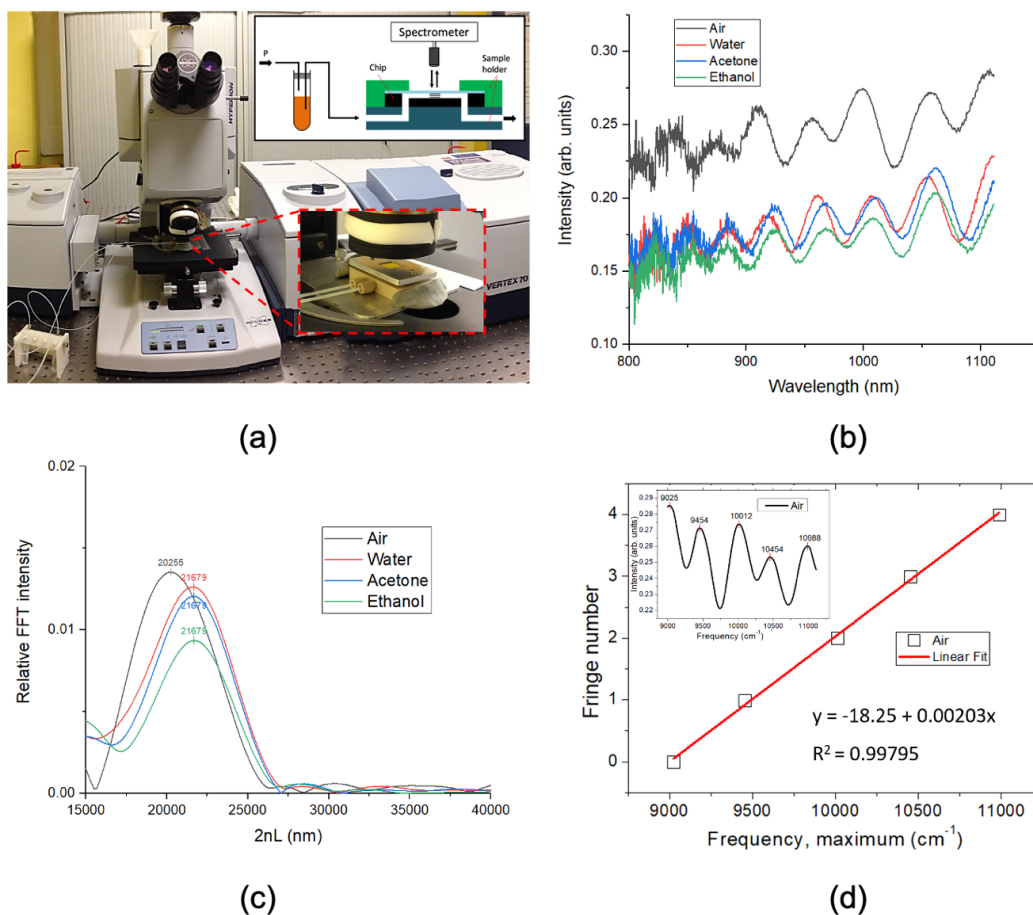
Figure 5. (a) Experimental setup for the acquisition of reflectance spectra of packaged LPSi chips filled with various solvents. (b) Reflectance spectra for a LPSi implanted membrane filled with different solvents (water, acetone, and ethanol). The spectrum marked as Air means that no liquid fills the pores. (c) RIFTS of the reflectance spectra of the LPSi membrane filled with different solvents. (d) Fringe number as a function of corresponding frequency, the inset shows the spectrum for the LPSi membrane filled with air replotted in frequency unit and the peaks of the interference pattern corresponding to successive peak numbers.

In addition to using the RIFTS method to analyze the Fabry-Pérot fringes in order to derive EOT (Fig. 5c), we have also fitted the spectra data using equation 1: the spectral order of each fringe (peak number) was plotted as a function of frequency and the slope of the linear fit provided the effective optical thickness (Fig. 5d). Only the first 5 peaks were selected because the spectrum contained overwhelming noise at high frequency.

Table S1 lists the experimental EOT values obtained from both analysis methods and the corresponding derived indices of refraction of the porous layer (n_{layer}), along with theoretical values

obtained using equation 2, with P = 40%, $n_{skeleton}$ = 3.673 [18] and using values of refractive indices of filling medium at 830 nm and 20 °C [19]. Results provided in Table S1 indicate that the experimental values are in good agreement with the theoretical ones. The composite refractive index values obtained using the linear fitting method are in the adequate order of air < water < acetone ≈ ethanol, which, indeed, corresponds to the shifts of measured interference patterns. However, we find that the RIFTS method cannot help distinguishing the different solvents used in the experiments. We thus used a third analysis method called Interferogram Average over Wavelength (IAW) recently proposed for the analysis of porous silicon interferometer spectra [20]. This method, which relies on the calculation of the average value over wavelength of spectral interferograms, was used to compare the acetone and ethanol data of Fig. 5b. Briefly, the interferograms were obtained by subtracting the reflection intensity of acetone and ethanol spectra from the Air spectrum used as a reference, removing the average value and applying the absolute value function (see Supporting Information Fig. S2). The IAW values were then obtained by integrating the interferogram amplitude in the wavelength range. The IAW values for ethanol and acetone are respectively 4.24 and 3.82, and illustrate a difference in spectra for the filling solvents that can indeed be discriminated.

Next, the sensitivity of the LPSi interferometer was estimated from the experimental shift of the maximum peak at 910.1 nm. We observed a 51.3 nm shift of the interference spectrum after filling the chip with water. This shift corresponds to a sensitivity of $\Delta\lambda/\Delta n_{fill} \approx$ 156 nm/RIU (refractive index unit), which is in the same range as the sensitivity of other vertical porous silicon interferometers reported in the literature, *e.g.* 78 nm/RIU [21], 140 nm/RIU [22] and up to 425 nm/RIU [23]. Since the spectral resolution of our apparatus (4 cm^{-1}) translates into a 0.3 nm wavelength resolution at 900 nm, the corresponding limit of detection is estimated to be 2 x 10^{-3} RIU. This limit of detection could be lowered to 6 x 10^{-4} RIU using an improved set-up with 0.1 nm resolution [24]. Although the sensitivity of porous silicon sensors is significantly lower than that of surface plasmon resonance sensors, porous silicon displays a high surface area that could offer other advantages for biosensing [25].

We have estimated the theoretical sensitivity of our device by means of simulation using Essential Macleod simulation tool taking into account the thicknesses and the optical indices of each layer present in the vertical stack. To this aim, the interference spectra for a homogeneous porous silicon layer with similar properties (thickness, porosity, refractive index) was plotted for various refractive index filling media (Fig. S3 in the Supporting Information). The simulated spectra shift at 845 nm is 44 nm when n_{fill} changes from 1 to 1.1, leading to a theoretical sensitivity of 440 nm/RIU. This is almost a threefold increase compared to the experimental sensitivity. We suggest that this discrepancy could

originate from the lack of homogeneity of the porous layer in terms of thickness, porosity and pore size, as can be seen in Fig. 3.

Last, we have investigated the possibility of increasing device performances with the use of advanced optical multilayer structures. Indeed, rather than simple porous layers, microcavities and rugate filters are known to provide sharp spectral features and sensors with high quality (Q) factors [26]. Even if the device sensitivity is independent of the Q factor, a better Q improves the confidence and reliability in resolving smaller resonance shifts [23]. Such advanced architectures that rely on the integration of dielectric layers are fairly easy to fabricate with VPSi layers since they can be made up with alternating layers of different porosities to modulate the refractive indices [25]. This can simply be achieved by modulating the current density during porous silicon anodization through the thickness of the silicon wafer. In our case, because we are creating the porous silicon in a lateral fashion, we cannot use this simple trick. However, we can easily pattern thin films with various refractive indices, *e.g.* silicon dioxide and silicon nitride, on top of the porous silicon membrane to create a dielectric distributed Bragg mirror (DBR) made of several pairs of alternating high and low index quarter-wave layers. As a matter of fact, we could also imagine, after encapsulating the microchannels and membranes with the glass cover, etching the handle wafer to release the structure and report it onto a substrate hosting another dielectric mirror, thus sandwiching the LPSi between 2 similar (SiO_2/Si_3N_4) Bragg mirrors. We acknowledge that it surely would be much more complicated to implement. Still, we have used simulation to study the impact of the integration of 3.5 pairs of alternating 105 nm silicon nitride and 146 nm silicon dioxide layers. The corresponding spectra are shown in Fig. 6 and, as expected display narrower fringes that are potentially more sensitive to a small refractive index change and that would enable to create LPSi interferometers with improved performances.
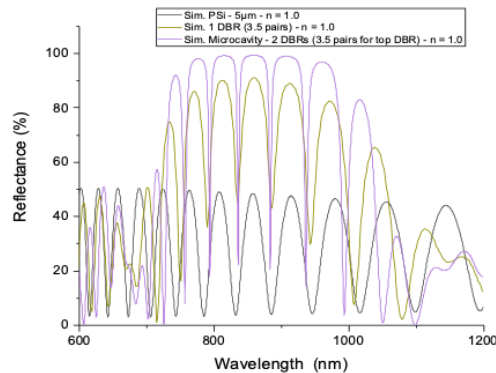

Figure 6. Simulated reflectance spectrum of a 5 µm thick implanted lateral porous silicon layer (black curve). Similar spectra when a dielectric 3.5× (SiO_2/Si_3N_4) mirror is added on top of the porous layer

(yellow curve) and when two similar mirrors are integrated on top and bottom of the LPSi layer (purple curve).

4. Conclusions

In summary, we have demonstrated the Fabry-Pérot interferometric transduction capability of fabricated lateral porous silicon membranes in a flow-through configuration, which differs from the flow-over configuration classically encountered with porous silicon layers with vertical pores. Interference signals were obtained using Fourier-transform infrared spectroscopy on lateral porous silicon membranes fabricated using two distinct processes, and despite the significant level of spectral noise due to the small footprint of the membranes, we were able to extract convincing porosity and index of refraction values. Additionally, spectral shifts were observed after filling a membrane with different solvents. Analysis of the spectra using various methods led to the determination of the index of refraction of the filling medium with a sensitivity of $\Delta\lambda/\Delta n_{fill} \approx 156$ nm/RIU and a limit of detection of 2 x 10^{-3} RIU. The discrepancy between the experimental sensitivity and the 440 nm/RIU theoretical sensitivity obtained by simulation is believed to be due to the inhomogeneity of the porous layer. However, these simulation works also demonstrated that the addition of Bragg mirrors on the membrane results in spectra displaying narrower fringes and devices with higher quality factors. We believe that this preliminary work paves the way toward alternative solutions for monolithically integrated flow-through biosensors if lateral porous silicon membranes are properly biofunctionalized.

References

[1] G. Luka *et al.*, "Microfluidics Integrated Biosensors: A Leading Technology towards Lab-on-a-Chip and Sensing Applications," *Sensors*, vol. 15, no. 12, pp. 30011–30031, Dec. 2015, doi: 10.3390/s151229783.
[2] E. K. Sackmann, A. L. Fulton, and D. J. Beebe, "The present and future role of microfluidics in biomedical research," *Nature*, vol. 507, no. 7491, pp. 181–189, Mar. 2014, doi: 10.1038/nature13118.
[3] L. Nicu and T. Leïchlé, "Biosensors and tools for surface functionalization from the macro- to the nanoscale: The way forward," *J. Appl. Phys.*, vol. 104, no. 11, p. 111101, Dec. 2008, doi: 10.1063/1.2973147.

[4] S. M. Borisov and O. S. Wolfbeis, "Optical Biosensors," *Chem. Rev.*, vol. 108, no. 2, pp. 423–461, Feb. 2008, doi: 10.1021/cr068105t.

[5] S. Dhanekar and S. Jain, "Porous silicon biosensor: Current status," *Biosens. Bioelectron.*, vol. 41, pp. 54–64, Mar. 2013, doi: 10.1016/j.bios.2012.09.045.

[6] G. Shtenberg and E. Segal, "Porous Silicon Optical Biosensors," in *Handbook of Porous Silicon*, L. Canham, Ed. Cham: Springer International Publishing, 2014, pp. 1–11. doi: 10.1007/978-3-319-04508-5_87-1.

[7] A. Janshoff *et al.*, "Macroporous p-Type Silicon Fabry–Perot Layers. Fabrication, Characterization, and Applications in Biosensing," *J. Am. Chem. Soc.*, vol. 120, no. 46, pp. 12108–12116, Nov. 1998, doi: 10.1021/ja9826237.

[8] L. De Stefano *et al.*, "Integrated silicon-glass opto-chemical sensors for lab-on-chip applications," *Sens. Actuators B Chem.*, vol. 114, no. 2, pp. 625–630, Apr. 2006, doi: 10.1016/j.snb.2005.05.027.

[9] C. Escobedo, A. G. Brolo, R. Gordon, and D. Sinton, "Flow-Through vs Flow-Over: Analysis of Transport and Binding in Nanohole Array Plasmonic Biosensors," *Anal. Chem.*, vol. 82, no. 24, pp. 10015–10020, Dec. 2010, doi: 10.1021/ac101654f.

[10] Y. Zhao, G. Gaur, R. L. Mernaugh, P. E. Laibinis, and S. M. Weiss, "Comparative Kinetic Analysis of Closed-Ended and Open-Ended Porous Sensors," *Nanoscale Res. Lett.*, vol. 11, no. 1, Dec. 2016, doi: 10.1186/s11671-016-1614-3.

[11] Y. Zhao, G. Gaur, S. T. Retterer, P. E. Laibinis, and S. M. Weiss, "Flow-Through Porous Silicon Membranes for Real-Time Label-Free Biosensing," *Anal. Chem.*, vol. 88, no. 22, pp. 10940–10948, Nov. 2016, doi: 10.1021/acs.analchem.6b02521.

[12] N. Kumar, E. Froner, R. Guider, M. Scarpa, and P. Bettotti, "Investigation of non-specific signals in nanoporous flow-through and flow-over based sensors," *The Analyst*, vol. 139, no. 6, p. 1345, 2014, doi: 10.1039/c3an01996a.

[13] R. Vercauteren, G. Scheen, J.-P. Raskin, and L. A. Francis, "Porous silicon membranes and their applications: Recent advances," *Sens. Actuators Phys.*, vol. 318, p. 112486, Feb. 2021, doi: 10.1016/j.sna.2020.112486.

[14] T. Leïchlé and D. Bourrier, "Integration of lateral porous silicon membranes into planar microfluidics," *Lab. Chip*, vol. 15, no. 3, pp. 833–838, 2015, doi: 10.1039/C4LC01094A.

[15] Y. He and T. Leïchlé, "Fabrication of lateral porous silicon membranes for planar microfluidics by means of ion implantation," *Sens. Actuators B Chem.*, vol. 239, pp. 628–634, Feb. 2017, doi: 10.1016/j.snb.2016.08.035.

[16] M. J. Sailor, *Porous silicon in practice: preparation, characterization and applications*. Weinheim: Wiley-VCH, 2012.

[17] C. Pacholski, M. Sartor, M. J. Sailor, F. Cunin, and G. M. Miskelly, "Biosensing Using Porous Silicon Double-Layer Interferometers: Reflective Interferometric Fourier Transform Spectroscopy," *J. Am. Chem. Soc.*, vol. 127, no. 33, pp. 11636–11645, Aug. 2005, doi: 10.1021/ja0511671.

[18] D. E. Aspnes and A. A. Studna, "Dielectric functions and optical parameters of Si, Ge, GaP, GaAs, GaSb, InP, InAs, and InSb from 1.5 to 6.0 eV," *Phys. Rev. B*, vol. 27, no. 2, pp. 985–1009, Jan. 1983.

[19] J. Rheims, J. Köser, and T. Wriedt, "Refractive-index measurements in the near-IR using an Abbe refractometer," *Meas. Sci. Technol.*, vol. 8, no. 6, pp. 601–605, Jun. 1997, doi: 10.1088/0957-0233/8/6/003.

[20] S. Mariani, L. Pino, L. M. Strambini, L. Tedeschi, and G. Barillaro, "10 000-Fold Improvement in Protein Detection Using Nanostructured Porous Silicon Interferometric Aptasensors," *ACS Sens.*, vol. 1, no. 12, pp. 1471–1479, Dec. 2016, doi: 10.1021/acssensors.6b00634.

[21] D. Ge, J. Shi, J. Wei, L. Zhang, and Z. Zhang, "Optical sensing analysis of bilayer porous silicon nanostructure," *J. Phys. Chem. Solids*, vol. 130, pp. 217–221, Jul. 2019, doi: 10.1016/j.jpcs.2019.03.002.

[22] L. Bonanno, "Steric Crowding Effects on Target Detection in an Affinity Biosensor," p. 16, 2008.

[23] L. A. DeLouise, P. M. Kou, and B. L. Miller, "Cross-Correlation of Optical Microcavity Biosensor Response with Immobilized Enzyme Activity. Insights into Biosensor Sensitivity," p. 9.

[24] A. Keating, "Porous Silicon Diffraction Gratings," in *Handbook of Porous Silicon*, L. Canham, Ed. Cham: Springer International Publishing, 2014, pp. 1–10. doi: 10.1007/978-3-319-04508-5_84-1.

[25] A. Jane, R. Dronov, A. Hodges, and N. H. Voelcker, "Porous silicon biosensors on the advance," *Trends Biotechnol.*, vol. 27, no. 4, pp. 230–239, Apr. 2009, doi: 10.1016/j.tibtech.2008.12.004.

[26] B. Gupta, Y. Zhu, B. Guan, P. J. Reece, and J. J. Gooding, "Functionalised porous silicon as a biosensor: emphasis on monitoring cells in vivo and in vitro," *The Analyst*, vol. 138, no. 13, p. 3593, 2013, doi: 10.1039/c3an00081h.